A Weighted Guided Filtering-Based Multidomain Fusion Destriping Method

Yang Hong ⓘ, Peng Rao ⓘ, Yuxing Zhou ⓘ, and Yuke Zhang ⓘ, *Member, IEEE*

Abstract—An infrared camera is affected by the photon effect, temperature changes, time drift, and other factors when operating in orbit, which makes the ground nonuniformity correction coefficient invalid, resulting in nonuniformity stripes in the infrared images and restricting their practicality in further analysis and applications. The existing destriping methods often suffer from the loss of image details and artifact generation. To solve this problem, we proposed a weighted guided filtering-based multidomain fusion destriping approach that leverages the structural, directional, and spectral characteristics of stripe noise. First, we addressed the issue of artifacts caused by Fourier-domain filtering through an adaptive filtering approach that employs a variable threshold to minimize filtering-induced artifacts and obtain clearer guided images. Furthermore, capitalizing on the directional properties of wavelet decomposition effectively separates image information from stripe information. To integrate the advantages of both approaches, we employed a weighted guided filter to seamlessly fuse the guided image with the wavelet decomposition image. In terms of quantitative metrics, the proposed method generally beats the other five comparative methods, with significant improvements in image PSNR, SSIM, NIQE, and mean relative deviation (MRD), particularly for complex images where the enhancements were more pronounced. These experimental results collectively demonstrate the significant progress achieved by the proposed method in effectively reducing stripe noise, better preserving the original structural details of the image, and suppressing the occurrence of artifacts.*

Index Terms—Fourier transform, image fusion, stripe noise, thermal infrared, wavelet decomposition, weighted guided filtering (WGF).

I. INTRODUCTION

IN RECENT years, infrared remote sensing technology has made significant advancements, expanding its applications across various fields, such as urban management, environmental protection, and military operations. During orbit operation, however, the detector is affected by temperature, the photon effect, aging, and other factors, which can make the ground nonuniformity correction factor invalid, resulting in nonuniformity in the image. This nonuniformity typically manifests as fixed pattern noise [1]. Currently, this type of stripe noise exists mainly in either horizontal or vertical directions due to the fact that most of the sensor readout circuits are arranged in rows or columns [2], [3], [4], [5], [6]. The existence of nonuniformity noise has detrimental effects on image quality, diminishes the signal-to-noise ratio, and significantly influences subsequent processing tasks, such as target detection. Consequently, the correction of infrared image nonuniformity emerges as a crucial technology that profoundly impacts the performance of infrared imaging systems. This article primarily focuses on addressing the correction of nonuniformity caused by stripe noise. The primary objective was to devise an efficient approach for alleviating the detrimental impacts of stripe noise and enhancing the overall quality of infrared images.

Nonuniformity correction methods can be broadly divided into two types: source-based methods and scene-based methods. Source-based methods primarily rely on observing a uniform reference standard, such as a blackbody, to correct for nonuniformities in imaging results. These methods offer high correction accuracy and operate on a relatively simple principle, making them the most commonly employed technique in infrared imaging [1]. Nevertheless, the effectiveness of this method of calibration is affected by time as well as temperature changes. On the other hand, scene-based methods primarily start from the assumption that stripe noise constitutes fixed noise. By analyzing continuously changing scenes, these methods identify and extract the constant components, namely the fixed noise. This principle renders them immune to variations in time and temperature. However, these methods necessitate scenes with significant motion, as the absence of motion may result in erroneous extraction of static structures as stripes, subsequently appearing in subsequent frames [7], [8], [9], [10], [11]. To address the challenges posed by multiframe methods, recent research efforts have been dedicated to developing single-frame destriping methods, which can be classified primarily into statistical-based methods [12], [13], [14], [15], [16], optimization-based methods [3], [17], [18], and filtering methods [19], [20], [21], [22], [23], [24], [25]. Statistical-based stripe removal methods involve analyzing the statistical features of an image to estimate and remove stripes. Statistical-based methods include histogram matching [13], [14] and moment matching [12], [16], [26] methods, which utilize the distribution of pixel intensities or statistical moments, respectively, to identify and eliminate stripe patterns

in an image. However, these methods are constrained by their initial assumptions, leading to inconsistent performance when dealing with different types of stripes and a limited robustness of the methods [15]. The optimization-based approach is employed to address the challenge of stripe removal by formulating it as an optimization problem. The objective function is iteratively minimized to achieve the desired outcome of reducing stripe intensity or eliminating stripes. These methods can be categorized into three primary classes: full variational methods [17], [27], [28], [29], low-rank methods [3], [5], [30], [31], and sparse constraint methods [32], [33], [34], [35], [36]. Although these methods exhibit strong adaptability and achieve effective destriping results, they are limited by their high computational complexity.

The filtering method designs a suitable filter to eliminate stripes according to their characteristics in the spatial or transform domain. Cao et al. [22] proposed a way to estimate noise stripes in the spatial domain using 1-D guided filtering (GF). The method of stripe removal in the transform domain has also received tremendous attention and research in recent years. These methods take the advantage of the properties of stripes in the transform domain for better stripe removal. In the Fourier domain, David et al. [37] employed a directional super-Gaussian function as a Fourier filter for stripe filtering. In a similar vein, Zeng et al. [38] introduced a spectral fusion approach that involved GF after identifying stripes through anomaly detection in the Fourier domain. Furthermore, Cao et al. [24] presented a method for filtering images at various scales after wavelet decomposition. However, such methods may inadvertently filter out image edges or information that shares the same characteristics as the stripe frequency, leading to image blurring or the introduction of artifacts. To address this issue, several scholars have proposed combined domain filtering methods to integrate different domains and mitigate the associated limitations [19], [39], [40], [41]. Because different types of noise may be more easily identified and addressed in different domains, multidomain fusion methods can more comprehensively remove noise while preserving important image features. Furthermore, dual-domain destripe methods typically exhibit good adaptability, allowing for the adjustment of destripe strategies based on the characteristics of different images and types of stripes.

To achieve superior destriping results, maximize the preservation of image details, and suppress artifacts, this study incorporates spatial processing techniques into the transform domain. Specifically, we propose a weighted guided filtering-based multidomain fusion destriping method. In the first stage, adaptive filtering in the Fourier domain is applied to the noisy image to derive a preliminary guided image. Next, wavelet decomposition is performed on both the guided and noisy images. Then, adaptive weighted guided filtering is used to fuse the low-frequency and stripe orientation components. This is followed by wavelet reconstruction to achieve a secondary guided image. Finally, the original image and the image obtained in the second stage are further fused using an adaptive weighted guided filtering method. The adaptive weighted guided filtering, by analyzing the horizontal and vertical gradient differences of

the image to estimate the intensity of stripe noise, optimizes the filtering strength of the weighted guided filtering, achieving efficient noise suppression and edge preservation. Therefore, the proposed method effectively addresses the issues of image detail loss and the introduction of artifacts. Furthermore, the implementation of our proposed method is much simpler and easier to implement. In this article, we mainly take the vertical stripes as an example, and the horizontal stripes can be processed by rotating the image.

Our contributions can be summarized in threefold.

1) We propose an improved Fourier-domain adaptive filtering (FDAF) method that identifies and substitutes the direct current (dc) values with abnormalities using mean values.
2) Building on the weighted guided filtering, we introduce a mechanism that dynamically adjusts filtering strength based on global gradient differences, effectively integrating both local and global information within images. This method potentially achieves superior fusion outcomes in complex scenarios compared with traditional methods.
3) We have incorporated the aforementioned methods into a multidomain fusion method for stripe removal and have successfully demonstrated the efficacy and robustness of our proposed method on multiscenario infrared remote sensing satellite images.

II. MATERIALS AND METHODS

We introduce a comprehensive approach to destriping that integrates three key components: FDAF, wavelet decomposition, and adaptive weighted guided filtering. As depicted in Fig. 1, our method incorporates a schematic diagram to illustrate its overall framework. Initially, the FDAF and wavelet decomposition techniques are employed to obtain a fringe correspondence diagram, serving as a guide image with vertical or horizontal components. The utilization of FDAF not only enhances the clarity of guided images but also enhances the efficiency of destriping while mitigating the generation of artifacts. Subsequently, a wavelet component fusion strategy based on the weighted guided filtering is applied, effectively merging the original image with the wavelet-derived component information from the guide image. A detailed exposition of each component of the method is provided in the following text.

A. Fourier-Domain Adaptive Filtering

The Fourier transform facilitates the conversion of an image from the spatial domain to the frequency domain, where each element in the Fourier image represents a specific frequency component in the original spatial domain image. This transformation enables the analysis and manipulation of different frequency components to extract valuable information and perform various image-processing tasks effectively. In order to remove stripes noise, generalized frequency filtering is used to equalize the dc values in each column of the Fourier transform. The most common method is to directly set the dc value to a constant, such as zero [39]. However, this method causes ringing artifacts, especially at the edge of the image, where the gray scale of
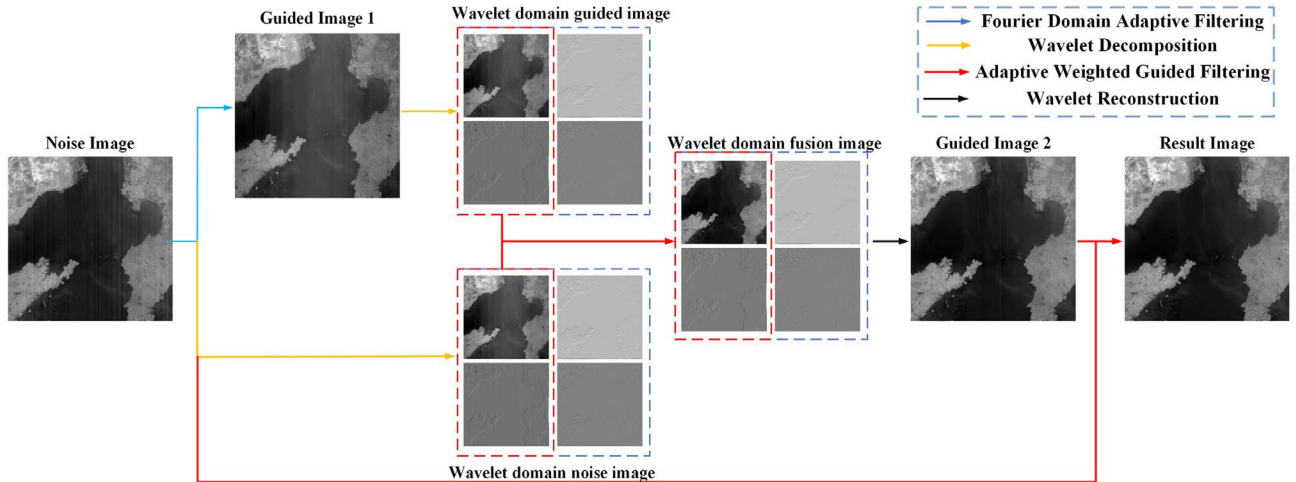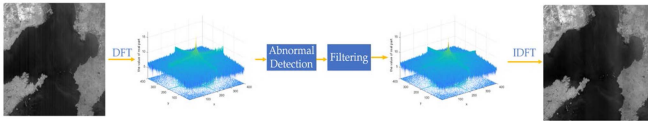
Fig. 1. Flowchart of our proposed method.

Fig. 2. Flowchart of FDAF.

the image changes drastically. Therefore, in order to address the issue of ringing artifacts and obtain better guided images, this article introduces an improved adaptive filtering approach. Inspired by the FDAF method proposed by Pande-Chhetri and Abd-Elrahman [19], our method has been modified to better suit our application scenario. Specifically, our method identifies and substitutes the dc values with abnormalities using mean values. In the Fourier domain, we first create a collection of columns that may be considered abnormal by evaluating if the difference between the dc value of the Fourier transform in any given column and the average value of the real parts for the rest of that column exceeds a predetermined threshold. If deemed abnormal, we then substitute the dc value of these columns with the average value of the remaining real parts

$$F_{\text{DC}}^j \in F_{\text{an}} \text{ if } \left| F_{\text{DC}}^j - \overline{F_{\text{real}}}^j \right| > k * F_{\sigma}^j \tag{1}$$

$$F_{\text{New\_DC}}^j = \begin{cases} \overline{F_{\text{real}}}^j, & j \in F_{\text{an}} \\ F_{\text{DC}}^j, & else \end{cases} \tag{2}$$

where F_{DC}^j denotes the dc values in column j, $\overline{F_{\text{real}}}^j$ is the mean value of the real parts in the rest of column j, F_{an} is the dc value in columns with abnormal values, k is a coefficient threshold used to judge abnormal values, and F_{σ}^j is the standard deviation of real parts in the rest of column j. The flowchart of the FDAF method is depicted in Fig. 2. The adaptive Fourier filtering method can effectively reduce the generation of artifacts so that a cleaner guided image is obtained. Although there may still be some low-frequency wide stripes present, they can be effectively eliminated by the subsequent use of weighted guided filtering.

B. Wavelet Decomposition

Wavelet decomposition is a signal-processing technique used to decompose signals into approximate and detailed components at different scales [19]. This is based on a set of wavelet function bases that have localized properties and are capable of capturing the local features of signals. The process of wavelet decomposition can be achieved by multistage filtering and downsampling [43]. At each scale level, the image wavelet transform is represented by one scaling function and three directionally sensitive wavelet functions [40]

$$\varphi(x, y) = \varphi(x)\varphi(y) \tag{3}$$

$$\psi^H(x, y) = \psi(x)\varphi(y) \tag{4}$$

$$\psi^V(x, y) = \varphi(x)\psi(y) \tag{5}$$

$$\psi^D(x, y) = \psi(x)\psi(y) \tag{6}$$

where $\varphi(x,y)$ represents the scaling function and $\psi^H(x, y)$, $\psi^V(x, y)$, and $\psi^D(x, y)$ represent the directional wavelet functions in the horizontal, vertical, and diagonal directions, respectively. This representation allows for efficient analysis of both global and local image features across different scales, making it a versatile tool for various image-processing applications.

Image multilevel wavelet decomposition can obtain low- and high-frequency components at different scales, manifesting as four component diagrams of different scales: the approximation component, horizontal component, vertical component, and diagonal component, as shown in Fig. 3. This particular characteristic of wavelet decomposition makes it highly effective in distinguishing stripes from image information. In the context of the destripe method, the primary emphasis lies on the components corresponding to the stripe direction and low-frequency image components, significantly preserving the image information in other components.

By utilizing these functions, wavelet decomposition can be performed, resulting in different scale low- and high-frequency components. This characteristic allows wavelet decomposition
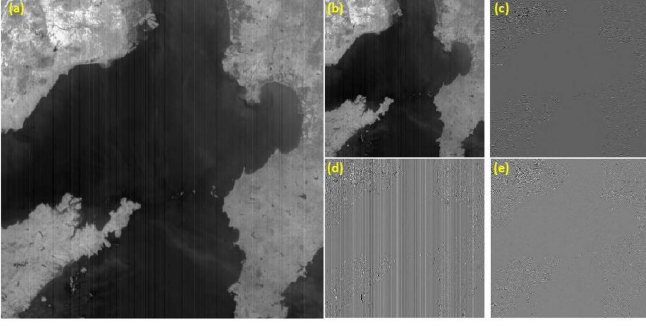
Fig. 3. (a) Stripe image. (b) Approximation component. (c) Horizontal component. (d) Vertical component. (e) Diagonal component.

to effectively separate edges from image information. In the context of stripe removal, the focus is on the components corresponding to the direction of the stripes and the approximation component. This approach can largely preserve the image information of other components. In general, the wavelet-based image filtering process involves three primary steps [19]:

1) decomposing the image by using a wavelet function at a specified scale level;
2) treating the components associated with the stripe direction;
3) reconstructing the image.

By following these steps, the wavelet-based approach efficiently removes the unwanted stripes while retaining important image features in other components. This method has found widespread applications in various image-processing domains, effectively enhancing image quality. However, this method still has the potential to filter out nonstripe information in the stripe direction component, and some wavelet deblurring methods appear to introduce artifacts in the edge region of the image.

Accordingly, this article primarily capitalizes on the characteristics of wavelet decomposition to disentangle the original image and the image obtained through adaptive filtering in the Fourier domain. This process effectively separates the stripe component from the image component. Subsequently, a weighted guided filtering technique is employed to enhance the preservation of fine image details and mitigate the occurrence of artifacts. This approach ensures superior protection of image intricacies and helps to avoid the generation of spurious effects.

C. Adaptive Weighted Guided Filtering

The GF algorithm is a better edge-preserving filtering algorithm, which can avoid the disadvantage of gradient inversion when using bilateral filtering algorithms [41].

The output image is

$$q_i = a_k I_i + b_k \forall i \in \omega_k \tag{7}$$

$$q_i = p_i - n_i \tag{8}$$

where p is the input image, I is the guide map, q is the output image, ω_k is the window centered at k, and a_k and b_k are the transformation coefficients assumed to be constant in ω_k. In GF, the output image q is considered to be the outcome of a local linear variation of the guided image I. Furthermore, the input image p is assumed to be the result of adding noise n to the output image q.

The coefficient of variation can be obtained by minimizing the gap between p and q. Therefore, a loss function E is defined as follows:

$$E(a_k, b_k) = \sum_{i \in \omega_k} \left((a_k I_i + b_k - p_i)^2 + \epsilon a_k{}^2 \right) \tag{9}$$

where the ϵ regularization parameter is introduced to prevent the resulting a_k from being too large; then, the linear ridge regression method is used to find the a_k and b_k that minimize the loss function

$$a_k = \frac{\frac{1}{|\omega|} \sum_{i \in \omega_k} I_i p_i - \mu_k \bar{p}_k}{\sigma_k^2 + \epsilon} \tag{10}$$

$$b_k = \bar{p}_k - a_k \mu_k \tag{11}$$

where μ_k is the mean value of the guided function in the window, $\bar{p}_k$ is the mean value of the input image within the window, $|\omega|$ is the number of pixels in the window, and σ_k^2 is the variance of the guided image within the window. However, the regularization parameter ϵ in the GF is constant, which leads to blurred edges and ghosting. In order to address this problem, the weighted guided filtering (WGF) introduces an edge-aware weighting $\Gamma_{i'}$ into the GF to enable adaptive adjustment of the image within the window through the regularization parameter ϵ [44]. As a result, the loss function E can be rewritten as follows:

$$E(a_k, b_k) = \sum_{i \in \omega_k} \left((a_k I_i + b_k - p_i)^2 + \frac{\epsilon}{\Gamma_{i'}} a_k{}^2 \right). \tag{12}$$

An edge-aware weighting $\Gamma_{i'}$ is defined as follows:

$$\Gamma_{i'} = \frac{1}{N} \sum_{i=1}^{N} \frac{\sigma_{i'}^2 + \varepsilon}{\sigma_i^2 + \varepsilon} \tag{13}$$

$$\varepsilon = (0.001 \times L)^2 \tag{14}$$

where N is the total number of image pixels, $\sigma_{i'}^2$ is the intrawindow variance, σ_i^2 is the overall image variance, and L is the image dynamic range. The constant ε is mainly used to prevent the case where $\Gamma_{i'}$ is zero, leading to an infinite loss function E. At this point, the transformation coefficients a_k and b_k are defined as follows:

$$a_k = \frac{\frac{1}{|\omega|} \sum_{i \in \omega_k} I_i p_i - \mu_k \bar{p}_k}{\sigma_k^2 + \frac{\epsilon}{\Gamma_{i'}}} \tag{15}$$

$$b_k = \bar{p}_k - a_k \mu_k. \tag{16}$$

When the window is at the edge, the intrawindow variance $\sigma_{i'}^2$ is larger than the overall image variance σ_i^2, and thus, $\Gamma_{i'}$ is larger than 1. If the intrawindow variance $\sigma_{i'}^2$ is smaller than the overall image variance σ_i^2 when the window is in the smooth region, then $\Gamma_{i'}$ is smaller than 1. Compared with the smooth area, the image weight for the window at the edge is greater, which can help protect edge information and reduce the blurring of the edge during filtering. Therefore, the fused output

image is

$$q_i = \frac{\frac{1}{|\omega|}\sum_{i\in\omega_k} I_i p_i - \mu_k \bar{p}_k}{\sigma_k^2 + \frac{\epsilon}{\Gamma_{i'}}} * I_i + \bar{p}_k - a_k\mu_k \tag{17}$$
$$\forall i \in \omega_k$$

where the guide image I specifically consists of the low-frequency component image and the high-frequency component image in the direction of the stripes, both obtained through wavelet decomposition after adaptive filtering in the Fourier domain. The input image p is the low-frequency component image and the high-frequency component image in the direction of the stripes, obtained from wavelet decomposition of the input noisy image.

Although weighted guided filtering can adjust the ϵ value locally through the image, the initial value of ϵ still needs to be determined based on the overall image stripe strength. When the intensity of the stripes is stronger, the large epsilon is needed, so we determine the intensity of the stripes by a simple method, i.e., the difference between the horizontal gradient and the vertical gradient, and when the difference is larger, which shows that the intensity of the stripes is stronger, we set a larger parameter

$$I_{\text{stripe}} = \left| \overline{\nabla_x I} - \overline{\nabla_y I} \right| \tag{18}$$

$$\epsilon = \begin{cases} 1, & I_{\text{stripe}} < \phi_1 \\ 3, & \phi_2 > I_{\text{stripe}} \geq \phi_1 \\ 5, & \phi_3 > I_{\text{stripe}} \geq \phi_2 \\ 10, & \phi_4 > I_{\text{stripe}} \geq \phi_3 \\ 20, & I_{\text{stripe}} \geq \phi_4 \end{cases} \tag{19}$$

where $\overline{\nabla_x I}$ represents the mean of the gradient values of the image in the horizontal direction, $\overline{\nabla_y I}$ denotes the mean of the gradient values in the vertical direction, and $\phi_i (i=1,2,3,4)$ represents the threshold of gradient difference.

Therefore, this article presents a novel approach that exploits the properties of adaptive weighted guided filtering to combine the component information from the original image with the corresponding wavelet components extracted from the guide image. This method ensures improved preservation of image information across the respective components, resulting in better overall image quality and an enhanced destripe performance.

III. EXPERIMENTAL RESULTS AND ANALYSIS

In this section, to evaluate our method, we used simulation data as well as actual images to assess its performance across various scenarios. In the meantime, we compared our method with five typical algorithms, including the wavelet Fourier adaptive filter (WFAF) [19], unidirectional total variational (UTV) [17], 1-D weighted least-squares filter (1D-WLS) [42], sheared low rank (SLR) [43], and WGF [44]. Moreover, we systematically examined the effects of different parameter values, such as threshold parameter (k), wavelet types, and wavelet decomposition levels (L), on the efficiency of stripe removal. By conducting these experiments and analyses, we gained valuable insights into the behavior of the proposed method using various parameter settings, facilitating the selection of optimal parameters for practical applications. The experimental results were analyzed quantitatively and qualitatively to assess the quality of
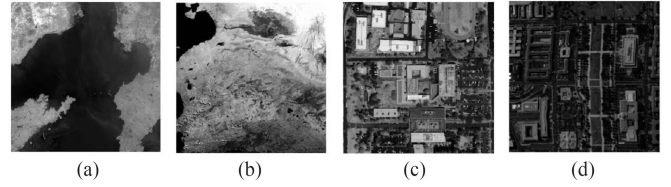

Fig. 4. Clear images for simulation experiment. (a) Image of Terra MODIS band 32. (b) Image of Aqua MODIS band 7. (c) Image of IKONOS. (d) Image of Washington DC Mall.

the processed images, namely the method's effectiveness. The qualitative assessment focuses on whether the destriped image produces artifacts or whether the image is distorted. The main evaluation methods are the visual appearance and the average value of the vertical profile of the images, the latter being used to display the brightness variations and noise levels along a specific row or column in the image [3], [17]. This facilitates a better observation of the stripe removal effect and helps to identify potential image detail loss. Indicators for quantitative analysis select peak signal-to-noise ratio (PSNR) [45], structural similarity (SSIM) [46], naturalness image quality evaluator (NIQE) [47], [48], and mean relative deviation (MRD) [49], [50]. The evaluation indices for simulated images were mainly used: PSNR and SSIM, where PSNR was primarily used to describe pixel value gaps between images, while SSIM was used to measure similarities between two images. For real images that did not have a reference image available, we choose NIQE and MRD parameters to quantify the perceived quality of an image by analyzing its natural nature [51]. In this section, we set the filter radius R to 10 and the adaptive Fourier filter threshold parameters are set to $k = 2$. In addition, we set the threshold of gradient difference $\phi_i (i = 1,2,3,4)$ to [2, 6, 10, 15].

A. Simulated Stripe Image

In our simulation experiments, we chose the publicly available MODIS images [52], a high-resolution city image taken by IKONOS [53] and the hyperspectral image of Washington DC Mall [54] as the clear images, as shown in Fig. 4. To demonstrate the practicality of the method, two types of stripes were simulated, namely periodic stripes and nonperiodic stripes.

1) Periodic Stripes: In order to prove the performance of the proposed method in removing periodic stripes, we periodically placed five columns of stripe noise in each of the ten columns in a clear image. Fig. 5 shows the stripe removal results of the above methods in different scenes. As can be seen from 1c–4c of Fig. 5, the SLR method clearly causes blurring of the image. This effect is particularly evident in the areas highlighted by the red boxes in 3c and 4c of Fig. 5, where the method clearly removes the inherent vertical features of the image. In contrast, 1e–4e of Fig. 5 shows the persistence of distinct stripes, highlighting the limited effectiveness of WGF in removing periodic stripes. Although both UTV and WFAF are effective in removing streak noise, there are obvious artifacts (dark stripes) in the areas enclosed by the red boxes in Fig. 5(3g), (4d), and (4g), compared with the original images. In the local zoomed-in image in Fig. 5(3f), it can be seen that a bright stripe is generated within the red circle,
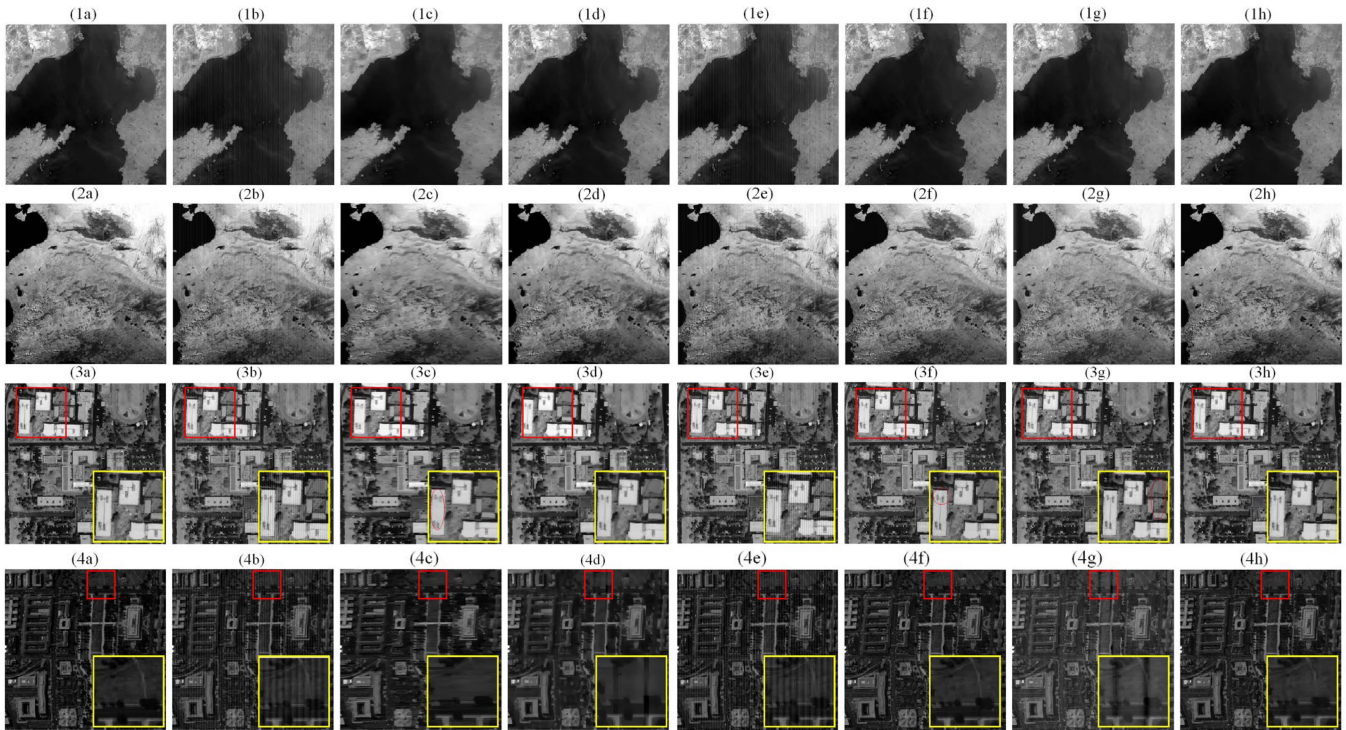
Fig. 5. Results for periodic stripe images. (a) Image devoid of stripes. (b) Periodic stripe image. (c) SLR. (d) UTV. (e) WGF. (f) 1D-WLS. (g) WFAF. (h) Our method.

which indicates that the 1D-WLS method also generates artifacts in some specific cases. In contrast, satisfactory results are obtained using the proposed method, which effectively preserves the image details without generating obvious artifacts.

2) Nonperiodic Stripes: To assess the efficacy of the proposed method in eliminating nonperiodic stripes, we introduced stripes of random intensity and position into the clear images.

Consistent with the findings from the periodic stripe test, Fig. 6 shows that both the proposed method and the 1D-WLS method have the most visually appealing results compared with other techniques. Fig. 6(1d), (4d), (3g), and (4g) of the nonperiodic stripe image test results demonstrates that the application of the UTV and WFAF methods results in the presence of noticeable artifacts in the region surrounded by the red box. Furthermore, the loss of image details is observed in (2c), (3c), and (4c) of Fig. 6, thereby confirming that the SLR method can lead to the loss of image details.

3) Qualitative Analysis: In addition, to further analyze the deblurring effect, we used a profile mean plot for comparison; Fig. 7 shows the image column mean curves of results for periodic stripe images, where the red curve represents the original image without stripes, and the blue curve represents the resulting image after processing. The vertical coordinate represents the average value of the vertical profile of the images, and the horizontal coordinate represents the column number in the image. In Fig. 7(1-4b) and (1-4d), the blue curves still display several discontinuous peaks. The blue curve in Fig. 7(1-4f) is oversmoothed in some areas compared with the original plot, which also produces abrupt changes in some columns. Moreover, the blue curve in Fig. 7(2c) still has several discontinuous

peaks, and in Fig. 7(4c), the blue curve is oversmoothed around the 150th column region. Overall, Fig. 7(1-4e) and (1-4g) show that 1D-WLS and our method have the best results in restoring the mean values of each column. In addition, as shown in Fig. 8, these two methods also perform best in terms of column mean recovery.

4) Quantitative Analysis: To further evaluate the outcomes, we introduced periodic striping of varying intensities into the images and conducted a quantitative assessment using PSNR and SSIM, as illustrated in Tables I and II. We have highlighted the best values in bold, and the amplitude represents the periodic stripe noise intensity. Scene 1 represents the image of MODIS band 32, Scene 2 represents the image of MODIS band 7, Scene 3 represents the city image captured by IKONOS, and Scene 4 represents the image of Washington DC Mall. As indicated in Table I, compared with other conventional approaches, our method demonstrated significant improvements in the PSNR metric for images containing periodic striped patterns, achieving a maximum enhancement of 58.6% and an average improvement of 32.3%. Similarly, for the SSIM metric, our method exhibited notable enhancements, with a maximum improvement of 191.1% and an average improvement of 42.2%. The results in Table I indicate that the proposed method exhibits superior performance in both metrics under various conditions. This is particularly evident in Scenes 3 and 4, where there is a notable improvement in the performance indicators, thereby more convincingly validating our method's suitability for images with denser details. However, in cases of high striping intensity, our method, although not the best, ranks second to the best performance. This highlights a limitation of our study, as the
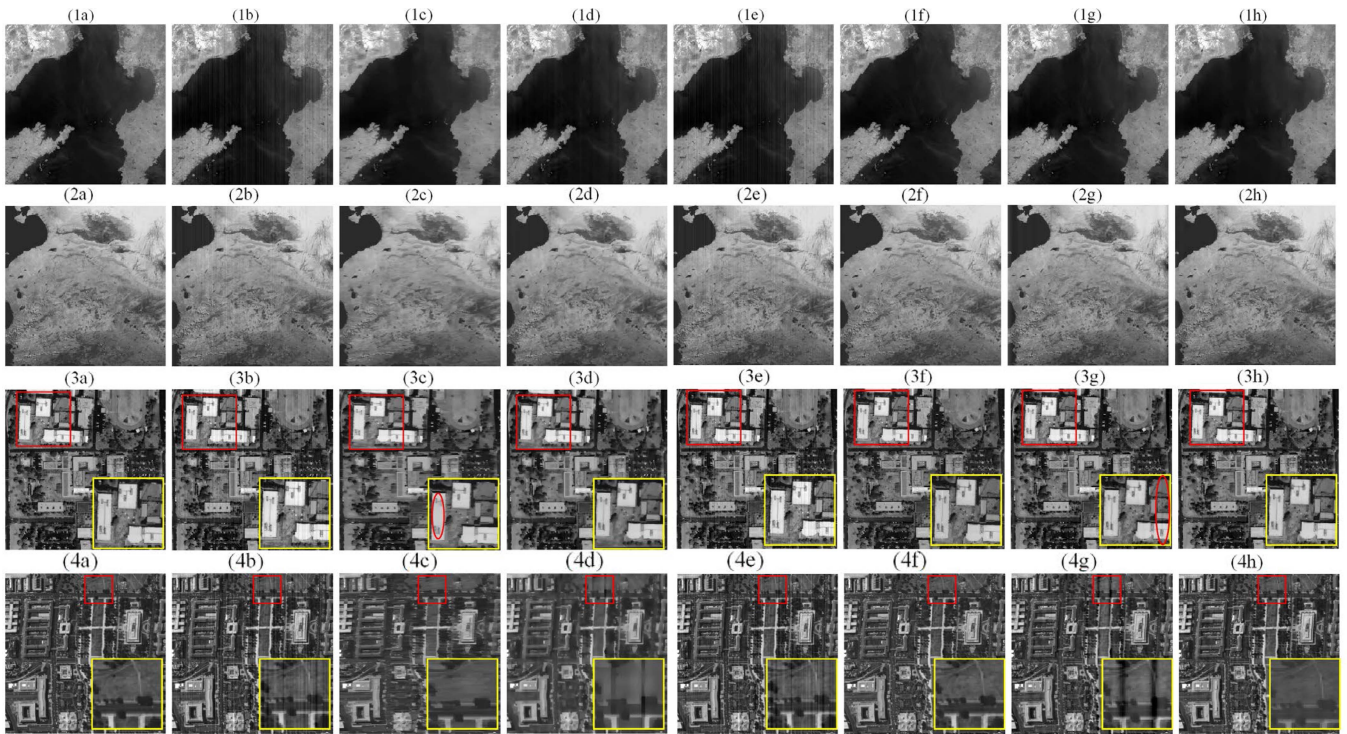
Fig. 6. Results for nonperiodic stripe images. (a) Image devoid of stripes. (b) Non-periodic stripe image. (c) SLR. (d) UTV. (e) WGF. (f) 1D-WLS. (g) WFAF. (h) Our method.
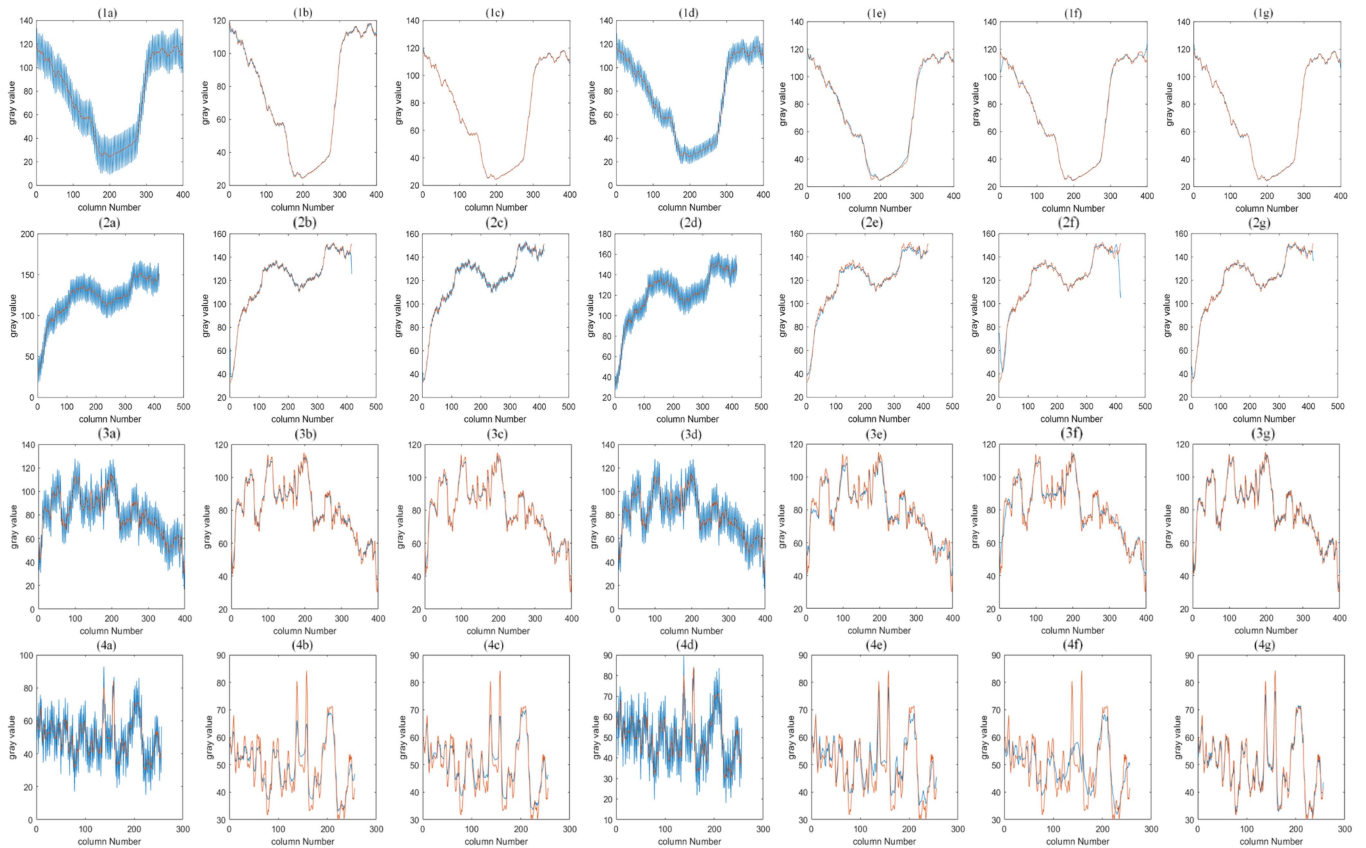

Fig. 7. Average value of the vertical profile of results for periodic stripe images. (a) Periodic stripes image. (b) SLR. (c) UTV. (d) WGF. (e) 1D-WLS. (f) WFAF. (g) Our method.
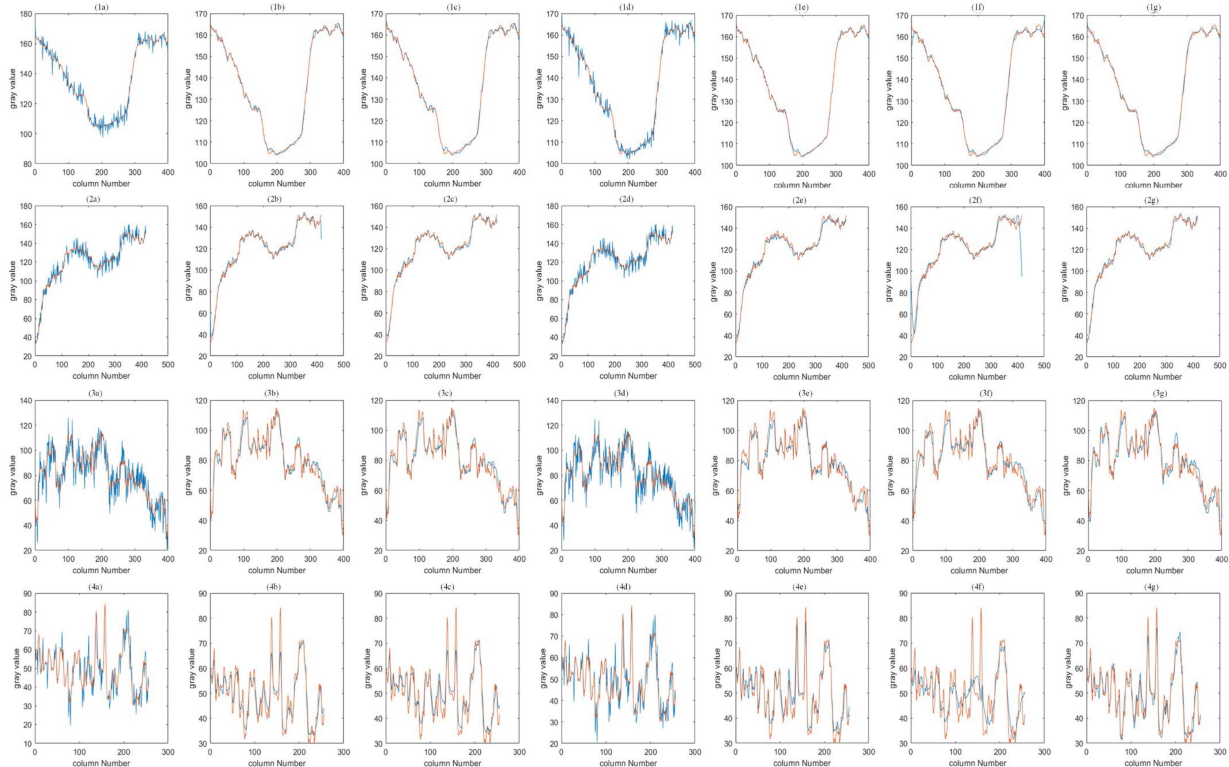
Fig. 8. Average value of the vertical profile of results for nonperiodic stripe images. (a) Nonperiodic stripes image. (b) SLR. (c) UTV. (d) WGF. (e) 1D-WLS. (f) WFAF. (g) Our method.

proposed method is more suited to situations with lower striping intensity.

From the results in Table II, it can be observed that our method also shows a better boosting effect in terms of the quantitative metrics when dealing with nonperiodic stripes. In comparison to the other conventional approaches, our method can achieve a maximum increase of 42.6% in the PSNR metric, with an average increase of 19.5%. Additionally, for the SSIM metric, our method has the potential to achieve a maximum enhancement of 22%, with an average improvement of 7.5%. However, in combination with the previous experimental results for periodic stripes, the PSNR and SSIM boosting effect of the proposed method in Scene 1 is suboptimal. This may be due to the fact that the stripes in Scene 1 have a specific structure and regularity with the original image, which may not match well with the processing of our method. Therefore, under different types of scenes, targeted adjustment of the algorithm parameters or other applicable methods may be required to further optimize the results. This indicates that our method may have some limitations in dealing with periodic and nonperiodic stripes, and thus needs to be carefully selected for use or improvement in specific application scenarios.

B. Real Stripe Image

In this section, we selected MODIS images and compact high-resolution imaging spectrometer (CHRIS) images [55]. The dataset consists of two images captured using a cross-track imaging system, exhibiting periodic stripe patterns, as shown in
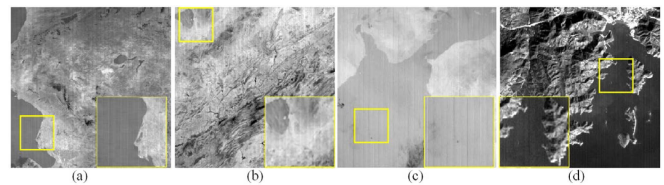

Fig. 9. Real images. (a) Image of terra MODIS band 30. (b) Image of aqua MODIS band 30. (c) Image of aqua MODIS band 32. (d) Image of CHRIS band 5.

Fig. 9(a) and (b). Additionally, there are two images obtained from a scanning imaging system, displaying nonperiodic stripe patterns, as depicted in Fig. 9(c) and (d). The chosen images were utilized to verify the practical applicability of the proposed method and to assess its performance in real-world scenarios.

Figs. 10 and 11 show a variety of methods for striping results and the corresponding average vertical profiles of the images. The results of the real-world image experiments are consistent with those obtained from the simulated experiments, with the exception of the stripe removal performance of Fig. 9(c), which is less satisfactory. Both Figs. 10 and 11 indicate that, for Fig. 9(c), the stripe removal results of almost all methods are unsatisfactory. This can be attributed to the limited grayscale variation within Fig. 9(c) and the prominent presence of strong stripes, which present a challenging situation for stripe removal methods. As a result, these methods struggle to differentiate between realistic image features and undesirable stripes, leading to a suboptimal performance across the various tested methods.
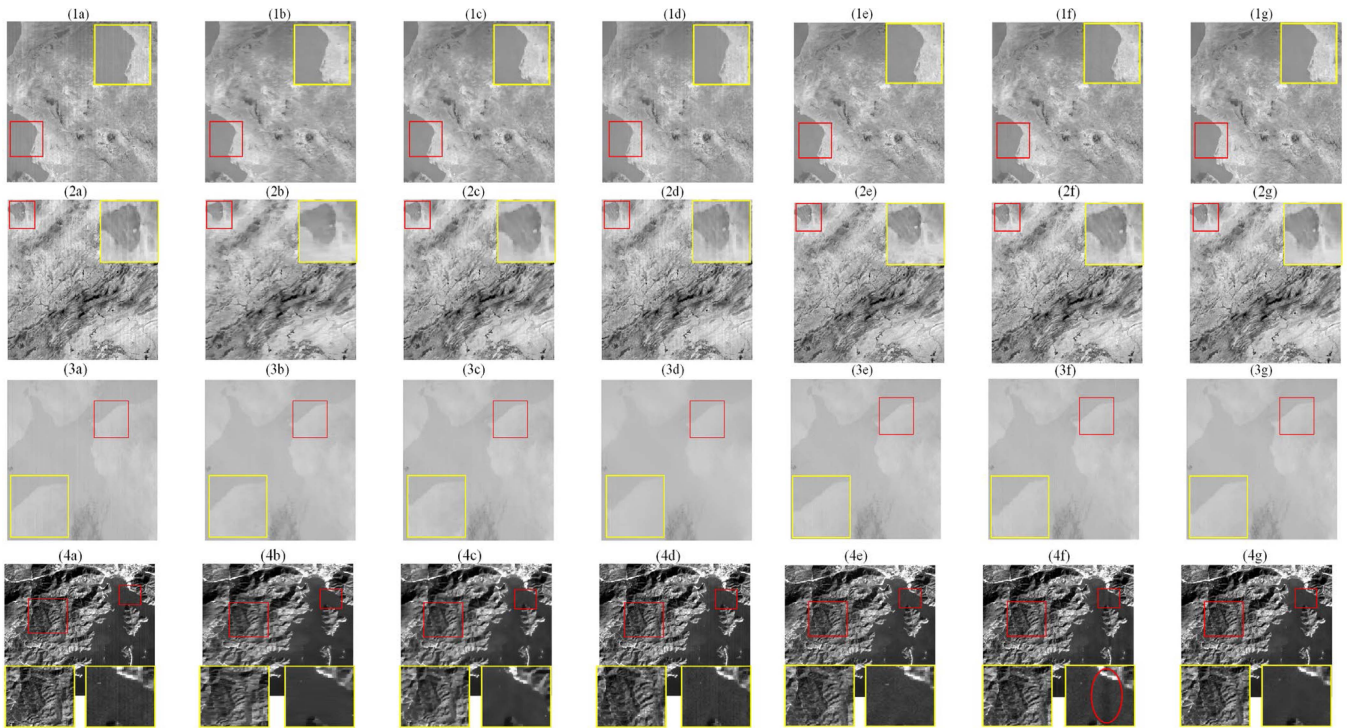
Fig. 10.   Results for real images. (a) Original image. (b) SLR. (c) UTV. (d) WGF. (e) 1D-WLS. (f) WFAF. (g) Our method.
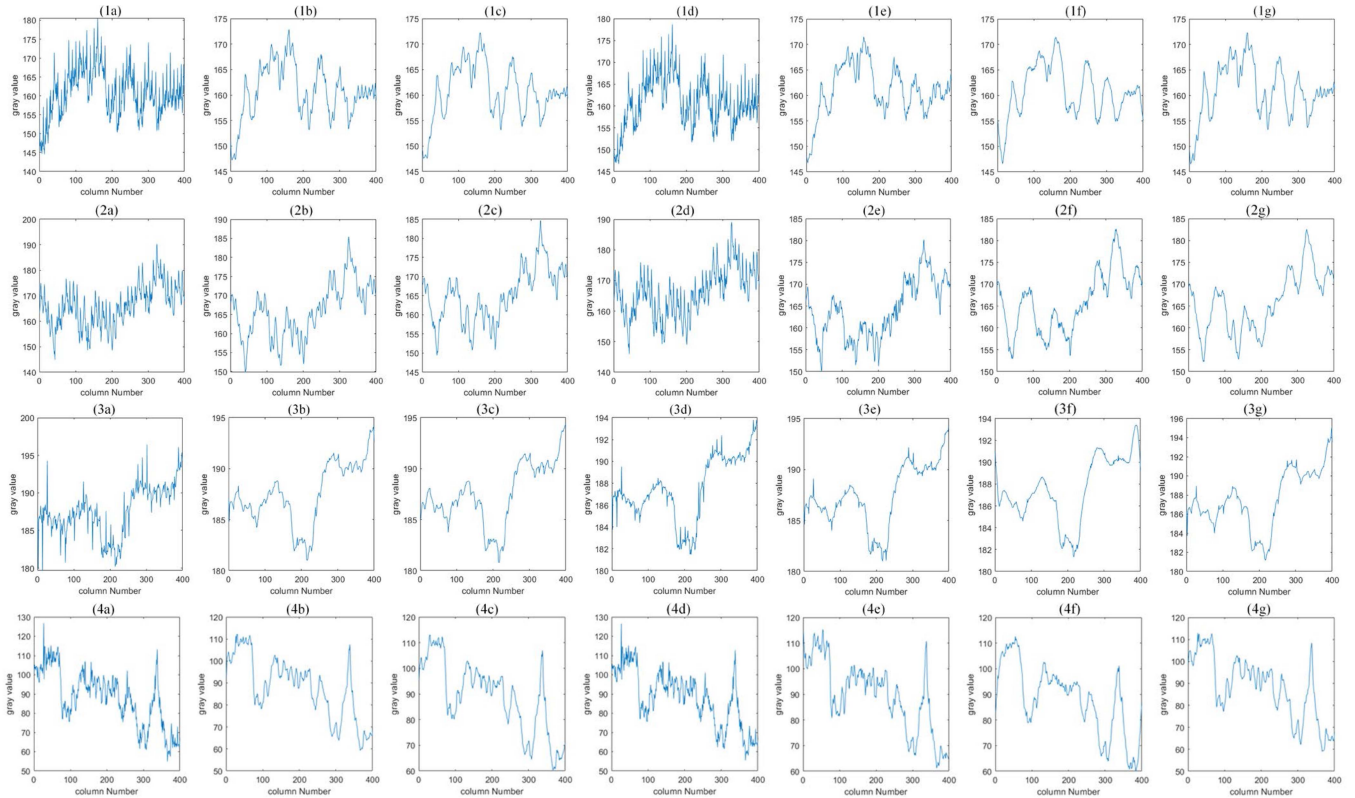

Fig. 11.   Average value of the vertical profile of results for real images. (a) Original image. (b) SLR. (c) UTV. (d) WGF. (e) 1D-WLS. (f) WFAF. (g) Our method.

TABLE I
PSNR (dB) AND SSIM FOR THE RESULTING IMAGES OF PERIODIC STRIPE IMAGES

Image	Method	Noise image							
		Intensity=10		Intensity=15		Intensity=20		Intensity=25	
		PSNR	SSIM	PSNR	SSIM	PSNR	SSIM	PSNR	SSIM
Scene 1	Noise image	31.126	0.845	27.915	0.733	25.715	0.633	22.459	0.339
	SLR	35.643	0.935	35.425	0.932	35.26	0.931	34.876	0.928
	UTV	41.677	0.974	38.323	0.951	35.994	0.92	35.081	0.987
	WGF	33.840	0.900	30.266	0.762	27.174	0.733	24.970	0.453
	1D-WLS	38.965	**0.996**	37.553	**0.996**	35.517	0.994	34.813	0.994
	WFAF	**42.752**	0.995	**42.752**	0.995	**42.752**	0.995	**41.299**	**0.994**
	Proposed	39.719	0.993	38.454	0.992	37.089	0.99	35.619	0.988
Scene 2	Noise image	32.19	0.889	28.978	0.836	26.779	0.78	25.13	0.724
	SLR	30.906	0.858	30.63	0.851	30.375	0.844	30.151	0.838
	UTV	35.142	0.924	34.186	0.907	33.185	0.888	32.024	0.863
	WGF	33.194	0.889	29.979	0.836	27.779	0.78	25.131	0.724
	1D-WLS	34.303	0.934	33.158	0.929	32.571	0.927	**32.104**	**0.925**
	WFAF	24.343	0.903	24.346	0.903	24.349	0.903	24.352	0.903
	Proposed	**36.378**	**0.936**	**34.338**	**0.932**	**33.508**	**0.928**	31.649	0.924
Scene 3	Noise image	28.821	0.881	26.003	0.792	23.965	0.708	22.402	0.633
	SLR	27.940	0.883	27.539	0.877	27.343	0.871	27.200	0.867
	UTV	30.300	0.917	30.317	0.918	30.325	0.918	30.297	0.918
	WGF	29.886	0.904	27.124	0.828	24.978	0.745	23.259	0.665
	1D-WLS	29.013	0.969	28.139	0.966	27.813	0.965	27.642	0.964
	WFAF	30.978	0.971	30.978	0.971	30.978	0.971	30.978	0.971
	Proposed	**34.878**	**0.988**	**34.755**	**0.987**	**31.932**	**0.981**	**31.512**	**0.980**
Scene 4	Noise image	28.031	0.835	24.767	0.719	22.554	0.617	20.907	0.531
	SLR	27.776	0.852	27.438	0.842	27.237	0.834	27.100	0.829
	UTV	26.858	0.826	26.946	0.826	27.038	0.827	27.132	0.827
	WGF	29.565	0.857	26.577	0.765	24.283	0.667	22.354	0.574
	1D-WLS	30.139	0.941	29.205	0.932	27.327	0.912	25.307	0.885
	WFAF	19.373	0.771	19.373	0.771	19.373	0.771	19.373	0.771
	Proposed	**33.224**	**0.966**	**33.069**	**0.963**	**30.376**	**0.945**	**31.220**	**0.949**

These results emphasize the necessity of paying attention to the specific features of the input images in the application of stripe elimination methods. The effectiveness of these methods can be significantly influenced by the overall grayscale variation of the image and the relative intensity of the existing stripes.

Next, we proceed with further comparative analysis of the results obtained from different stripe removal methods. In Fig. 10(1-4d), numerous stripes remain apparent, and in Fig. 11(1-4d), there are still numerous discontinuous peaks, indicating that the weighted guided filtering (WGF) does not exhibit a pronounced destriping effect. The observed artifacts within the red boxes in Fig. 10(4f) indicate that the WFAF introduces banding artifacts in scenarios where there is a significant contrast variation along the direction of the stripes. For instance, such artifacts may arise when pixel columns contain both bright land regions and relatively darker water regions simultaneously. From Fig. 10(4b) and (4c), it can be observed that, while the methods based on SLR and UTV effectively remove a significant

number of stripes, they also lead to blurring of the images. In comparison with the original image, the boundaries between land and sea in the image become blurred, and the regions within the red boxes also suffer from excessive blurring. Additionally, the areas within the red boxes in Fig. 10(1-3b) and (1-3c) also exhibit excessive smoothing effects. Upon applying the proposed method to Fig. 9(b) for stripe removal, Fig. 10(2g) demonstrates the proposed method's significant success in eliminating stripes. However, the curve in Fig. 11(2g) exhibits smooth transitioning around the 200th column region, which may be attributed to the method processing the high-frequency components of the image as well, causing some image detail loss. Based on the experimental results from these four images, the proposed method and the 1D-WLS method exhibit promising performances. While there might be some issues of excessive blurring or smoothing in certain regions, both methods demonstrate considerable effectiveness in stripe removal and superior preservation of image details. Moreover, they effectively reduce the

TABLE II
PSNR (dB) AND SSIM FOR THE RESULTING IMAGES OF NONPERIODIC STRIPE IMAGES

Image	Method	Noise image							
		Intensity=10		Intensity=15		Intensity=20		Intensity=25	
		PSNR	SSIM	PSNR	SSIM	PSNR	SSIM	PSNR	SSIM
Scene 1	Noise image	34.384	0.948	31.047	0.906	28.692	0.812	28.041	0.809
	SLR	35.945	0.939	35.405	0.936	35.123	0.932	35.460	0.934
	UTV	**44.828**	0.989	40.397	0.987	**40.544**	0.983	39.278	0.982
	WGF	36.968	0.975	32.755	0.937	30.200	0.868	30.096	0.811
	1D-WLS	40.680	**0.997**	34.625	**0.995**	37.323	**0.995**	35.737	**0.994**
	WFAF	40.991	0.994	**40.419**	0.993	39.900	0.993	**40.089**	**0.994**
	Proposed	41.206	0.987	37.599	0.973	33.675	0.921	39.998	0.987
Scene 2	Noise image	35.013	0.931	31.641	0.909	27.487	0.866	26.81	0.843
	SLR	31.167	0.863	31.018	0.859	30.552	0.841	30.384	0.834
	UTV	35.571	0.932	34.917	0.913	33.939	0.894	33.649	0.888
	WGF	36.440	0.932	32.096	0.909	28.376	0.872	28.305	0.865
	1D-WLS	34.525	0.935	33.913	0.933	33.449	0.931	**33.756**	**0.933**
	WFAF	25.912	0.912	25.962	0.913	25.686	0.91	25.828	0.91
	Proposed	**37.799**	**0.943**	**35.814**	**0.935**	**35.634**	**0.936**	31.257	0.922
Scene 3	Noise image	33.631	0.982	29.185	0.944	25.367	0.920	24.715	0.905
	SLR	28.617	0.892	28.399	0.885	28.176	0.887	28.061	0.886
	UTV	31.191	0.937	30.426	0.918	28.086	0.921	27.510	0.911
	WGF	33.643	0.982	32.927	0.966	25.747	0.919	28.087	0.929
	1D-WLS	35.122	**0.985**	32.544	0.979	30.243	0.973	32.142	0.978
	WFAF	29.734	0.965	29.979	0.967	30.211	0.968	30.052	0.968
	Proposed	**36.356**	0.984	**35.274**	**0.982**	**31.818**	**0.976**	**32.557**	**0.975**
Scene 4	Noise image	31.277	0.959	26.780	0.907	25.749	0.886	22.760	0.826
	SLR	28.036	0.871	27.595	0.865	28.036	0.866	27.691	0.858
	UTV	26.549	0.820	26.582	0.826	27.781	0.835	27.668	0.837
	WGF	31.440	0.944	28.211	0.910	26.068	0.880	22.942	0.822
	1D-WLS	29.087	0.938	29.529	0.941	28.929	0.935	27.937	0.923
	WFAF	19.346	0.770	19.321	0.770	19.655	0.778	19.904	0.783
	Proposed	**32.906**	**0.966**	**29.857**	**0.946**	**30.955**	**0.952**	**27.986**	**0.925**

TABLE III
MRD AND NIQE RESULTS OF THE TEST METHODS

Image		SLR	UTV	WGF	1D-WLS	WFAF	Proposed
Terra MODIS band 30	NIQE	6.590	3.590	5.784	3.093	3.099	**2.803**
	MRD	0.119	0.037	0.037	**0.032**	0.040	**0.032**
Aqua MODIS band 30	NIQE	6.871	4.809	4.185	3.432	3.743	**3.395**
	MRD	0.036	0.030	0.034	0.026	0.023	**0.021**
Terra MODIS band 32	NIQE	6.713	5.994	5.892	5.450	5.760	**4.757**
	MRD	0.015	0.020	0.015	0.014	0.018	**0.008**
CHRIS band 5	NIQE	7.163	5.119	5.266	5.383	5.374	**5.017**
	MRD	0.071	0.108	**0.0004**	0.034	0.087	0.048

occurrence of artifacts, further enhancing the quality of the images.

To provide a more comprehensive validation of the proposed method on realistic infrared images, we employed no-reference evaluation metrics, namely NIQE and mean relative difference (MRD), to quantitatively assess the images, and the results are listed in Table III. When considering real-world images, in comparison with the alternative comparative methods, our approach

demonstrates the potential to achieve a maximum improvement of 58% in the NIQE metric, with an average enhancement of 20.5%. Similarly, for the MRD metric, our method showcases the ability to achieve a maximum improvement of 75%, with an average enhancement of 22%. The results from the NIQE metrics demonstrate the satisfactory performance of the proposed methods. As for MRD, the proposed method exhibits a superior performance on periodic stripe images. It should be emphasized that, although the WGF method produces higher values for nonperiodic stripe images, there are still noticeable residual stripes present in the resulting processed images. Overall, the proposed method demonstrates better stripe removal capabilities compared with other methods and effectively preserves image details.

C. Parameter Analysis

The methods proposed in this study require that three parameters are adjusted during implementation:

1) the threshold of the Fourier adaptive filtering (k);
2) the type of wavelet transform;
3) the number of decomposition levels;
4) the threshold of gradient difference (ϕ_i).

Although one would also need to set the weighted guided filter radius parameters, this parameter can be adjusted for image complexity due to different image details. Generally, when the image has more details, the filter radius is selected in the range of 1–3, while when the image has fewer image details and the stripe width is wider, a larger filter radius of 5–15 can be selected. Threshold (k) values are employed to distinguish outliers and identify regions with high-contrast image information, thereby preventing the generation of image artifacts. Selecting a low k value means that more pixels are treated as effective high-frequency components in the image, while a higher k value allows manipulation of these pixels. For comparison experiments, the thresholds were set to 0.3, 0.5, 0.7, 1, 1.5, 1.8, 2, and 2.5. In fact, different types of wavelets have different effects on the wavelet decomposition and, consequently, the quality of stripe removal. Wavelet types commonly used for this purpose include Morlet wavelets, Mexican hat wavelets, Daubechies wavelets, Symlets wavelets, Coiflets wavelets, and others. Each wavelet has a different waveform, and their properties, such as symmetry, regularity, and compact support, are different. In this study, we mainly use different levels of Daubechies wavelets and different levels of Symlets wavelets for testing purposes (specifically db4, db8, sym5, and sym8). Each of these selected wavelet types provides unique advantages and characteristics for the wavelet decomposition process, allowing for a comprehensive evaluation and comparison of their effectiveness in stripe removal. Furthermore, the choice of the wavelet decomposition levels depends on the type of stripe. For instance, nonperiodic stripes tend to have more frequencies compared with periodic stripes, necessitating higher decomposition levels. In this study, we primarily conduct tests with decomposition levels L set to 2, 3, 4, 5, and 6. These different levels enabled us to explore the impact of various frequency components on the stripe removal process and ascertain the optimal decomposition level to effectively address different
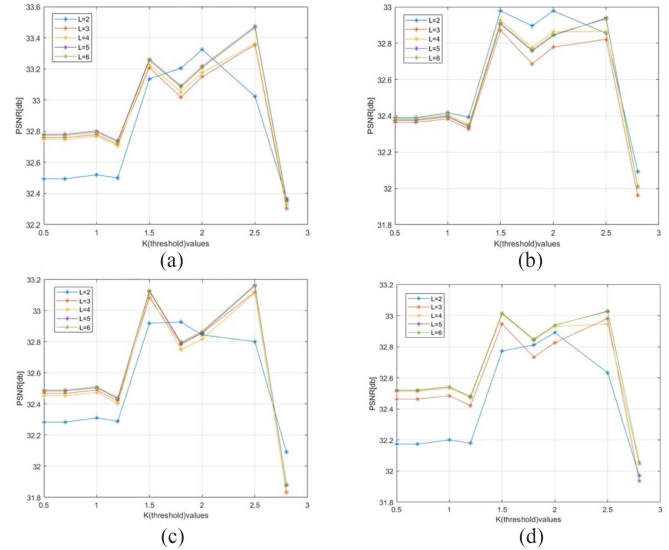

Fig. 12. Relationship between PSNR and the threshold values (k), considering various decomposition levels and wavelet types: (a) db4 wavelet; (b) db8 wavelet; (c) sym5 wavelet; and (d) sym8 wavelet, applied to the simulated nonperiodic stripe noise image of the Washington DC Mall.

types of stripe patterns. We chose a simulated nonperiodic stripe noise image of the Washington DC Mall as a representative example and selected the PSNR value as the evaluation metric, subsequently graphing the relationship between PSNR and the above three parameters.

From Fig. 12, it is evident that the optimal value for parameter k lies between 1.5 and 2.5. When k is smaller than 1.5, some image information might be mistakenly identified as stripes, leading to the destruction of the original structure of the image, thus reducing the PSNR. Conversely, when k exceeds 2.5, a larger k value may cause certain stripe noise to be erroneously classified as image details during thresholding, thus compromising the efficiency of the stripe removal. Furthermore, as the wavelet decomposition level increases, the PSNR increases in most cases, as shown in Fig. 12. However, when the wavelet decomposition level exceeds 4, the increase in PSNR becomes negligible. Therefore, we consider the optimal wavelet decomposition level to be in the range of 4–5. Higher decomposition levels would reduce computational efficiency without significantly improving the approach's performance. Finally, from Fig. 12, it is evident that selecting the "db4" wavelet type yields higher PSNR values. Overall, the trend in the curve in Fig. 12 indicates that, when k exceeds 1.2, the PSNR undergoes rapid changes with varying k values. This observation implies that the proposed stripe removal method is more sensitive to the threshold (k) compared with changes in wavelet type or wavelet decomposition level (L). The performance of our method is greatly affected by the selection of the k value, making it a critical parameter for achieving effective stripe removal results and optimizing image quality. Proper tuning and careful selection of the threshold k are vital to ensure the success of the stripe removal process in the proposed method.

Finally, in our investigation into the threshold of gradient difference ϕ_i, we conducted a series of experiments utilizing

TABLE IV
DIFFERENT COMBINATIONS FOR ABLATION STUDY AND RESULT

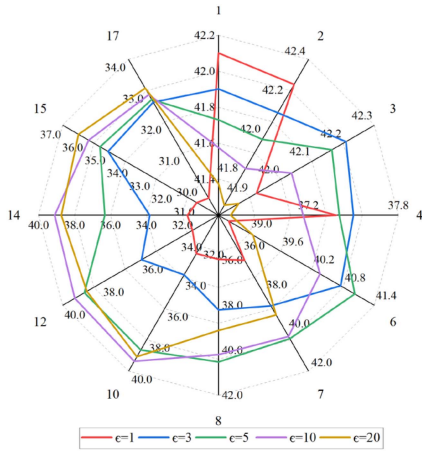| Method	Framework	Fourier Domian		Fusion Method			PSNR	SSIM
		DC = 0	FDAF	GF	WGF	AWGF		
Method 1	√	√				√	30.878	0.9385
Method 2	√		√	√			32.971	0.9488
Method 3	√		√		√		32.931	0.9490
Our Method	√		√			√	**33.144**	**0.9495**

Fig. 13. PSNR of results different ϵ values for varying stripe noise intensities.

sets of images with varying intensities of stripe noise (I_{stripe}) to evaluate the impact of different ϵ on the filtering outcome. The selection of threshold values was informed by these experiments, with the results, as depicted in Fig. 13. In this figure, the outer circle numbers indicate the I_{stripe} levels of stripe intensity, while different colored lines represent various ϵ values.

A meticulous examination of Fig. 13 reveals a pronounced correlation between the optimal ϵ values and the specific intervals of stripe intensities. More specifically, within the intensity ranges of [0–2], [2–6], [6–10], [10–15], and [15–17] as the ϵ values were sequentially set to 1, 3, 5, 10, and 20, the resultant images achieved the best PSNR values. Based on these findings, we have selected [2], [6], [10], and [15] as our reference points for threshold values, applying these in both our simulation experiments and real-image testing. These experiments yielded superior results, in previous sections, further validating the effectiveness of our approach in selecting thresholds for varying levels of stripe noise intensity.

D. Ablation Study

To rigorously ascertain the efficacy of the individual components within the proposed method, ablation studies were meticulously undertaken. The configurations for the control groups are delineated in Table IV, and the framework is depicted in Fig. 1. Specifically, Method 1 integrates a method where the dc value is set to zero (dc = 0), Method 2 adopts a conventional GF approach for the purpose of fusion, and Method 3 selected the weighted guided filtering (WGF) method for image fusion. These experiments were executed across a spectrum of images,

encompassing diverse scenes, categories, and varying degrees of stripe intensities, with scenes being selected from Fig. 4. The outcomes of these investigations are quantitatively evaluated and the results are systematically illustrated in Table IV and Fig. 14, providing a comprehensive insight into the performance implications of each method component. Columns 7 and 8 of Table IV present the average values of PSNR and SSIM across various scenarios. The data reveal that, on average, our method outperforms the existing methods, highlighting its overall effectiveness. Detailed comparisons for individual scenarios are further elaborated through Fig. 14, emphasizing the advantages of our approach.

Fig. 14 elucidates the comparative superior efficacy of our method over the other methods under scrutiny, as evidenced across a suite of eight diverse test images. A detailed examination of the results between Method 1 with our approach underscores a pronounced improvement, attributable to the implementation of our improved FDAF. Through comparative analysis of Method 2, Method 3, and our proposed AWGF method, the results demonstrate that our approach consistently outperforms the other two methods overall, especially in the processing of images 3 and 4. This further validates the effectiveness of the adaptivity of our method. However, when processing certain specific images, such as images 6 and 8, the performance of our method closely aligns with that of Method 3. This phenomenon occurs because, under these conditions, the filtering strength selected through our method's adaptivity mechanism coincidentally matches the fixed filtering strength used by Method 3, leading to similar processing outcomes on these specific images. This observation not only showcases the adaptive capabilities of our method but also reveals the potential consistency between adaptive and fixed parameter selections under certain circumstances.

IV. DISCUSSION

From both visual inspection and quantitative metrics, it is evident that the algorithm proposed in this article exhibits robust destriping capabilities while preserving the inherent structure of the images in the majority of scenarios. Especially in image scenes with complex details, our proposed method outperforms several other methods [17], [19], [42], [43], [44], as can be seen from the profile of Scenes 3 and 4 the results of the quantization metrics. For Scenes 3 and 4, whether periodic or nonperiodic stripes are added, the profile curves of this article's method are the closest to those of the clean image; in addition, from the analysis of the quantization metrics, this article's method
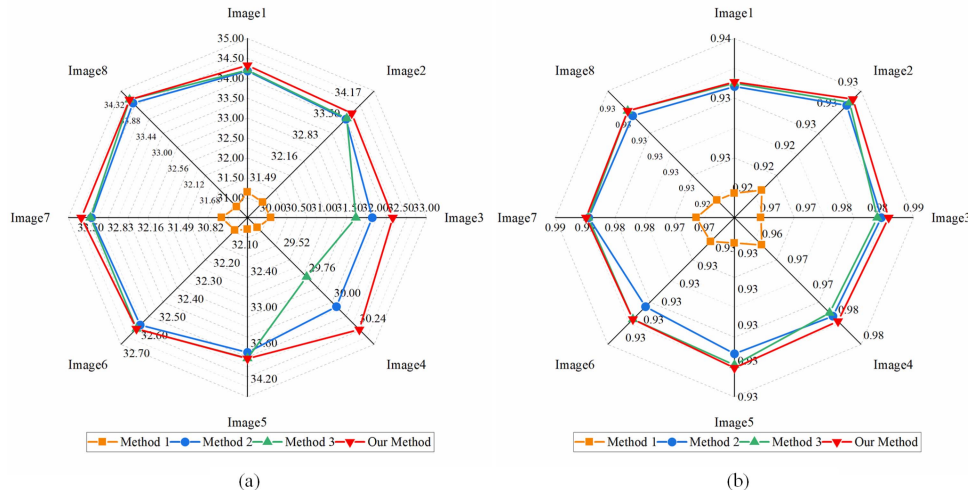
Fig. 14. Results for ablation study. (a) PSNR. (b) SSIM.

improves the PSNR by an average of 58% and the SSIM metrics by an average of 23.3%. This advantage can be attributed to the incorporation of a multilevel detail preservation approach in our algorithm, which effectively prevents the removal of subtle image features that might be inadvertently eliminated by other destriping methods. Furthermore, the comparative results from the ablation study clearly demonstrate the effectiveness of the proposed improvements in the Fourier domain and fusion method. The proposed method is superior to Method 1 in the ablation study, mainly due to the proposed mechanism for detecting and replacing outliers. Unlike the traditional Fourier-domain filtering that sets the dc component to a fixed value, the proposed approach allows for a more flexible handling of the dc value in the frequency domain. Inappropriate choices for the dc replacement value can lead to abrupt changes in image brightness, especially causing artifacts in areas of high contrast; however, the proposed method effectively avoids this issue. Similarly, compared with other fusion methods, our method is based on weighted guided filtering and introduces an innovative mechanism that leverages an analysis of the overall image gradient discrepancy to determine the intensity of stripe noise, thereby enabling dynamic adjustment of the filtering strength ϵ. This approach can adapt to the image's noise and texture characteristics on a global scale, thus more precisely balancing detail preservation and noise suppression during the weighted guided filtering process. By combining global optimization and local optimization strategies, this strategy offers more ideal fusion effects compared with traditional methods, especially in complex scenarios. Moreover, the proposed method, achieved by combining several simple methods, boasts low complexity and faster computational speed, offering the potential for significant contributions to the real-time processing of in-orbit satellite imagery.

However, we acknowledge that our method also has its limitations. In some cases, especially when dealing with images containing excessively prominent stripes, our algorithm might not achieve the optimal destriping performance. This could be an area for potential improvement in future research.

Additionally, a thorough analysis of the parameters involved in our algorithm was conducted. The experimental results from the parameter analysis indicated that setting the threshold (k) between 1.5 and 2.5, using a wavelet decomposition level (L) of 4–5, selecting the "db4" wavelet type, and selecting the threshold of gradient difference as [2], [6], [10], and [15] yielded the better destriping outcomes. However, for the parameters associated with adaptive weighted guided filtering, such as the filtering radius and blur coefficient, fine-tuning based on specific image characteristics is required to achieve optimal results.

In conclusion, the proposed method demonstrates superior destriping capabilities and image structure preservation, especially in scenarios with intricate details. Nevertheless, there exist certain limitations, particularly in cases of highly intense stripes, which might necessitate further research to address this. The parameter analysis provides valuable insights into achieving better performance, and careful adjustments of these parameters tailored to individual images can enhance the effectiveness of our algorithm. Overall, the findings support the practicality and efficacy of our proposed approach for destriping tasks while recognizing the need for continued refinements in specific scenarios.

V. CONCLUSION

In this article, we proposed a combined domain destriping method using weighted guided filtering. The method utilizes FDAF to obtain a clean and clear guidance image. Then, it employs wavelet decomposition to separate the image into different components. Finally, the stripe image and the guidance image are fused in the wavelet domain using weighted guided filtering. By integrating the advantages of spatial, wavelet, and frequency domain stripe removal techniques, our method enhances the destriping effect, preserves the original structural details of the image, and further reduces the introduction of artifacts through adaptive filtering and fusion. Through extensive experiments on both simulated and realistic images, we compared our method with five different destriping methods. Both visual inspection

and quantitative analysis revealed the clear advantages of our proposed approach. It effectively removes stripes while significantly preserving the original image details and successfully suppressing the occurrence of artifacts. However, the proposed method still has certain limitations, especially when dealing with uneven stripe information and excessively strong stripes, which calls for further improvements. In conclusion, our research presents an effective and versatile approach for stripe removal, but further refinements are required to address specific challenging scenarios encountered in the destriping process.

REFERENCES

[1] L. P. David and L. D. Eustace, "Linear theory of nonuniformity correction in infrared staring sensors," *Opt. Eng.*, vol. 32, no. 8, pp. 1854–1859, 1993, doi: 10.1117/12.145601.

[2] C. Lu, "Stripe non-uniformity correction of infrared images using parameter estimation," *Infrared Phys. Technol.*, vol. 107, Jun. 2020, Art. no. 103313, doi: 10.1016/j.infrared.2020.103313.

[3] Y. Chang, L. Yan, T. Wu, and S. Zhong, "Remote sensing image stripe noise removal: From image decomposition perspective," *IEEE Trans. Geosci. Remote Sens.*, vol. 54, no. 12, pp. 7018–7031, Dec. 2016, doi: 10.1109/TGRS.2016.2594080.

[4] J. Li, D. Zeng, J. Zhang, J. Han, and T. Mei, "Column-spatial correction network for remote sensing image destriping," *Remote Sens.*, vol. 14, no. 14, 2022, Art. no. 3376. [Online]. Available: https://www.mdpi.com/2072-4292/14/14/3376

[5] J. Zhang, X. Zhou, L. Li, T. Hu, and C. Fansheng, "A combined stripe noise removal and deblurring recovering method for thermal infrared remote sensing images," *IEEE Trans. Geosci. Remote Sens.*, vol. 60, Aug. 2022, Art. no. 5003214.

[6] E. Wang, Z. Liu, B. Wang, Z. Cao, and S. Zhang, "Infrared image stripe noise removal using wavelet analysis and parameter estimation," *J. Modern Opt.*, vol. 70, no. 3, pp. 170–180, Feb. 2023, doi: 10.1080/09500340.2023.2219775.

[7] L. Dong, W. Jin, and J. Sui, *Summarize on the Scene-Based Nonuniformity Correction Algorithms for IRFPA (Optics and Photonics)*. Cergy Pontoise, France: SPIE, 2005.

[8] A. Averbuch, G. Liron, and B. Z. Bobrovsky, "Scene based non-uniformity correction in thermal images using Kalman filter," *Image Vis. Comput.*, vol. 25, no. 6, pp. 833–851, 2007.

[9] D. Scribner, K. Sarkady, M. Kruer, J. Caulfield, J. Hunt, and C. Herman, *Adaptive Nonuniformity Correction for IR Focal-Plane Arrays Using Neural Networks*. Cergy Pontoise, France: SPIE, 1991.

[10] J. G. Harris and C. Yu-Ming, "Nonuniformity correction of infrared image sequences using the constant-statistics constraint," *IEEE Trans. Image Process.*, vol. 8, no. 8, pp. 1148–1151, Aug. 1999, doi: 10.1109/83.777098.

[11] W. Qian, Q. Chen, and G. Gu, "Space low-pass and temporal high-pass nonuniformity correction algorithm," *Opt. Rev.*, vol. 17, no. 1, pp. 24–29, 2010.

[12] F. Gadallah, F. Csillag, and E. Smith, "Destriping multisensor imagery with moment matching," *Int. J. Remote Sens.*, vol. 21, no. 12, pp. 2505–2511, 2000.

[13] M. Weinreb, R. Xie, J. Lienesch, and D. Crosby, "Destriping GOES images by matching empirical distribution functions," *Remote Sens. Environ.*, vol. 29, no. 2, pp. 185–195, 1989.

[14] B. K. Horn and R. J. Woodham, "Destriping Landsat MSS images by histogram modification," *Comput. Graph. Image Process.*, vol. 10, no. 1, pp. 69–83, 1979.

[15] J. Jia, X. Zheng, S. Guo, Y. Wang, and J. Chen, "Removing stripe noise based on improved statistics for hyperspectral images," *IEEE Geosci. Remote Sens. Lett.*, vol. 19, Oct. 2020, Art. no. 5501405, doi: 10.1109/LGRS.2020.3028443.

[16] P. Rakwatin, W. Takeuchi, and Y. Yasuoka, "Stripe noise reduction in MODIS data by combining histogram matching with facet filter," *IEEE Trans. Geosci. Remote Sens.*, vol. 45, no. 6, pp. 1844–1856, Jun. 2007.

[17] M. Bouali and S. Ladjal, "Toward optimal destriping of MODIS data using a unidirectional variational model," *IEEE Trans. Geosci. Remote Sens.*, vol. 49, no. 8, pp. 2924–2935, Aug. 2011, doi: 10.1109/TGRS.2011.2119399.

[18] Y. Chang, L. Yan, H. Fang, and H. Liu, "Simultaneous destriping and denoising for remote sensing images with unidirectional total variation and sparse representation," *IEEE Geosci. Remote Sens. Lett.*, vol. 11, no. 6, pp. 1051–1055, Jun. 2014, doi: 10.1109/LGRS.2013.2285124.

[19] R. Pande-Chhetri and A. Abd-Elrahman, "De-striping hyperspectral imagery using wavelet transform and adaptive frequency domain filtering," *ISPRS J. Photogramm. Remote Sens.*, vol. 66, no. 5, pp. 620–636, Sep. 2011, doi: 10.1016/j.isprsjprs.2011.04.003.

[20] Y. Shao et al., "Infrared image stripe noise removing using least squares and gradient domain guided filtering," *Infrared Phys. Technol.*, vol. 119, 2021, Art. no. 103968.

[21] E. Wang, P. Jiang, X. Li, and H. Cao, "Infrared stripe correction algorithm based on wavelet decomposition and total variation-guided filtering," *J. Eur. Opt. Soc.-Rapid Pub.*, vol. 16, 2020, Art. no. 1.

[22] Y. Cao, M. Y. Yang, and C.-L. Tisse, "Effective strip noise removal for low-textured infrared images based on 1-D guided filtering," *IEEE Trans. Circuits Syst. Video Technol.*, vol. 26, no. 12, pp. 2176–2188, Dec. 2015.

[23] J. J. Simpson, J. I. Gobat, and R. Frouin, "Improved destriping of GOES images using finite impulse response filters," *Remote Sens. Environ.*, vol. 52, no. 1, pp. 15–35, 1995.

[24] Y. Cao, Z. He, J. Yang, X. Ye, and Y. Cao, "A multi-scale non-uniformity correction method based on wavelet decomposition and guided filtering for uncooled long wave infrared camera," *Signal Process., Image Commun.*, vol. 60, pp. 13–21, 2018.

[25] Y. Cao, Z. He, J. Yang, Y. Cao, and M. Y. Yang, "Spatially adaptive column fixed-pattern noise correction in infrared imaging system using 1D horizontal differential statistics," *IEEE Photon. J.*, vol. 9, no. 5, Oct. 2017, Art. no. 7803513.

[26] P. Rakwatin, W. Takeuchi, and Y. Yasuoka, "Restoration of aqua MODIS band 6 using histogram matching and local least squares fitting," *IEEE Trans. Geosci. Remote Sens.*, vol. 47, no. 2, pp. 613–627, Feb. 2008.

[27] M. Wang, X. Zheng, J. Pan, and B. Wang, "Unidirectional total variation destriping using difference curvature in MODIS emissive bands," *Infrared Phys. Technol.*, vol. 75, pp. 1–11, 2016.

[28] A. Boutemedjet, C. Deng, and B. Zhao, "Edge-aware unidirectional total variation model for stripe non-uniformity correction," *Sensors*, vol. 18, no. 4, 2018, Art. no. 1164.

[29] T. Hu, W. Li, N. Liu, R. Tao, F. Zhang, and P. Scheunders, "Hyperspectral image restoration using adaptive anisotropy total variation and nuclear norms," *IEEE Trans. Geosci. Remote Sens.*, vol. 59, no. 2, pp. 1516–1533, Feb. 2020.

[30] J.-H. Yang, X.-L. Zhao, T.-H. Ma, Y. Chen, T.-Z. Huang, and M. Ding, "Remote sensing images destriping using unidirectional hybrid total variation and nonconvex low-rank regularization," *J. Comput. Appl. Math.*, vol. 363, pp. 124–144, 2020.

[31] Y. Chang, L. Yan, X.-L. Zhao, H. Fang, Z. Zhang, and S. Zhong, "Weighted low-rank tensor recovery for hyperspectral image restoration," *IEEE Trans. Cybern.*, vol. 50, no. 11, pp. 4558–4572, Nov. 2020.

[32] E. Pan, Y. Ma, X. Mei, F. Fan, J. Huang, and J. Ma, "Progressive hyperspectral image destriping with an adaptive frequencal focus," *IEEE Trans. Geosci. Remote Sens.*, vol. 61, Aug. 2023, Art. no. 5517312, doi: 10.1109/TGRS.2023.3297622.

[33] J. Song, J. H. Jeong, D. S. Park, H. H. Kim, D. C. Seo, and J. C. Ye, "Unsupervised denoising for satellite imagery using wavelet directional CycleGAN," *IEEE Trans. Geosci. Remote Sens.*, vol. 59, no. 8, pp. 6823–6839, Aug. 2021, doi: 10.1109/TGRS.2020.3025601.

[34] Y. Chang, L. Yan, L. Liu, H. Fang, and S. Zhong, "Infrared aerothermal nonuniform correction via deep multiscale residual network," *IEEE Geosci. Remote Sens. Lett.*, vol. 16, no. 7, pp. 1120–1124, Jul. 2019, doi: 10.1109/LGRS.2019.2893519.

[35] P. Xiao, Y. Guo, and P. Zhuang, "Removing stripe noise from infrared cloud images via deep convolutional networks," *IEEE Photon. J.*, vol. 10, no. 4, 2018, Art. no. 7801114, doi: 10.1109/JPHOT.2018.2854303.

[36] J. Luo, R. Wang, M. Ban, and X. Nan, "Fixed pattern noise removal for solar images using a self-supervised destriping network," in *Proc. IEEE 7th Inf. Technol. Mechatron. Eng. Conf.*, 2023, pp. 1571–1578, doi: 10.1109/ITOEC57671.2023.10291961.

[37] T. L. David, B. Marouan, A. Aaron, F. Reuben, and V. Gianluca, "Efficient destriping of remote sensing images using an oriented super-Gaussian filter," in *Proc. Image Signal Process. Remote Sens.*, 2020. Art. no. 1153306, doi: 10.1117/12.2574449.

[38] Q. Zeng, H. Qin, X. Yan, and T. Yang, "Fourier domain anomaly detection and spectral fusion for stripe noise removal of TIR imagery," *Remote Sens.*, vol. 12, no. 22, 2020, Art. no. 3714. [Online]. Available: https://www.mdpi.com/2072-4292/12/22/3714

[39] Z. Zhang, Z. Shi, W. Guo, and S. Huang, "Adaptively image destriping through frequency filtering," in *Proc. Opt. Inf. Process.*, 2006, pp. 989–996.

[40] W. Z. Yang, Z. H. Liu, S. L. Wang, and S. K. Lu, "Destriping line-scan color image in transform domain," in *Proc. Int. Conf. Comput. Sci. Appl.*, 2015, pp. 90–94, doi: 10.1109/CSA.2015.31.

[41] K. He, J. Sun, and X. Tang, "Guided image filtering," in *Proc. Eur. Conf. Comput. Vis.*, 2010, pp. 1–14.

[42] F. Li, Y. Zhao, and W. Xiang, "Single-frame-based column fixed-pattern noise correction in an uncooled infrared imaging system based on weighted least squares," *Appl. Opt.*, vol. 58, no. 33, pp. 9141–9153, Nov. 2019, doi: 10.1364/AO.58.009141.

[43] J.-L. Wang, T.-Z. Huang, T.-H. Ma, X.-L. Zhao, and Y. Chen, "A sheared low-rank model for oblique stripe removal," *Appl. Math. Comput.*, vol. 360, pp. 167–180, Nov. 2019, doi: 10.1016/j.amc.2019.03.066.

[44] Z. Li, J. Zheng, Z. Zhu, W. Yao, and S. Wu, "Weighted guided image filtering," *IEEE Trans. Image Process.*, vol. 24, no. 1, pp. 120–129, Jan. 2015, doi: 10.1109/TIP.2014.2371234.

[45] A. Horé and D. Ziou, "Image quality metrics: PSNR vs. SSIM," in *Proc. IEEE 20th Int. Conf. Pattern Recognit.*, 2010, pp. 2366–2369, doi: 10.1109/ICPR.2010.579.

[46] Y. A. Al-Najjar and D. C. Soong, "Comparison of image quality assessment: PSNR, HVS, SSIM, UIQI," *Int. J. Sci. Eng. Res.*, vol. 3, no. 8, pp. 1–5, 2012.

[47] S. Li, Z. Yang, and H. Li, "Statistical evaluation of no-reference image quality assessment metrics for remote sensing images," *ISPRS Int. J. Geo-Inf.*, vol. 6, no. 5, 2017, Art. no. 133.

[48] K. Gao et al., "Image restoration for real-world under-display imaging," *Opt. Exp.*, vol. 29, no. 23, pp. 37820–37834, 2021.

[49] X. Lu, Y. Wang, and Y. Yuan, "Graph-regularized low-rank representation for destriping of hyperspectral images," *IEEE Trans. Geosci. Remote Sens.*, vol. 51, no. 7, pp. 4009–4018, Jul. 2013, doi: 10.1109/TGRS.2012.2226730.

[50] H. Shen and L. Zhang, "A MAP-based algorithm for destriping and inpainting of remotely sensed images," *IEEE Trans. Geosci. Remote Sens.*, vol. 47, no. 5, pp. 1492–1502, May 2008.

[51] A. Mittal, R. Soundararajan, and A. C. Bovik, "Making a 'completely blind' image quality analyzer," *IEEE Signal Process. Lett.*, vol. 20, no. 3, pp. 209–212, Mar. 2013, doi: 10.1109/LSP.2012.2227726.

[52] LAADS Daac. 2024. [Online]. Available: https://ladsweb.nascom.nasa.gov

[53] 2020. [Online]. Available: https://www.isprs.org/data/ikonos/default.aspx

[54] Index of Hyperspectral Imagedata. 2024. [Online]. Available: https://engineering.purdue.edu/~biehl/MultiSpec/hyperspectral.html

[55] Brockmann Consult. 2010. [Online]. Available: http://www.brockmann-consult.de/beam/data/products/

Yang Hong received the B.S. degree in measurement and control technology and instrumentation from China Jiliang University, Hangzhou, China, in 2020. She is currently working toward the Ph.D. degree in electronic circuit and system with the Shanghai Institute of Technical Physics, Chinese Academy of Sciences, Shanghai, China.

Her research interests include infrared radiometric calibration and image processing.

Peng Rao received the Ph.D. degree with a major in photoelectric detection system from the University of Chinese Academy of Sciences, Beijing, China, in 2014.

He is currently a Professor with the Shanghai Institute of Technical Physics, Chinese Academy of Sciences, Shanghai, China. His research interests include photoelectric detection system and image processing.

Yuxing Zhou received the M.S. degree in optical engineering from the Harbin Institute of Technology, Harbin, China, in 2014.

He is currently with the Shanghai Institute of Technical Physics, Chinese Academy of Sciences, Shanghai, China. His research interests include infrared image calibration and processing.

Yuke Zhang (Member, IEEE) received the B.S. degree in electrical and information engineering from the Ocean University of China, Qingdao, China, in 2019. She is currently working toward the Ph.D. degree in electronic circuit and system with the Shanghai Institute of Technical Physics, Chinese Academy of Sciences, Shanghai, China.

Her research interests include image processing and infrared target enhancement.